Whole-brain fluorescence-MRI coregistration for precise anatomical mapping of virus infection

Nunya Chotiwan[1,2]*, Stefanie M. A. Willekens[1,2,3], Erin Schexnaydre[2,4,5], Max Hahn[3], Federico Morini[3], Jianguo Zhang[2,4,5,†], Emma Nilsson[1,2], Lars-Anders Carlson[2,4,5], Ulf Ahlgren[3], Daniel Marcellino[6], Anna K. Överby[1,2]*

Affiliations:

[1]Department of Clinical Microbiology, Umeå University; Umeå, Sweden.

[2]The laboratory for Molecular Infection Medicine Sweden (MIMS), Umeå University; Umeå, Sweden.

[3]Umeå Centre for Molecular Medicine (UCMM), Umeå University; Umeå, Sweden.

[4]Wallenberg Centre for Molecular Medicine, Umeå University; Umeå, Sweden.

[5]Department of Medical Biochemistry and Biophysics, Umeå University; Umeå, Sweden.

[6]Department of Integrative Medical Biology, Umeå University; Umeå, Sweden.

†Current address: Center for Biological Imaging, Institute of Biophysics, Chinese Academy of Sciences; Beijing, China

*Corresponding authors. E-mail: nunya.chotiwan@umu.se, anna.overby@umu.se

Abstract:

Neurotropic virus infections cause tremendous disease burden. Methods visualizing infection in the whole brain remain unavailable which greatly impedes understanding of viral neurotropism and pathogenesis. We devised an approach to visualize the distribution of neurotropic virus infection in whole mouse brain *ex vivo*. Optical projection tomography (OPT) signal was coregistered with a unique magnetic resonance imaging (MRI) brain template, enabling precise anatomical mapping of viral distribution, and the effect of type I interferon on distribution of infection was analyzed. Guided by OPT-MR, we show that Langat virus specifically targets sensory brain systems and the lack of type I interferon response results in an anatomical shift in infection patterns in the brain. We confirm this regional tropism, observed with whole brain OPT-MRI, by confocal and electron microscopy to provide unprecedented insight into viral neurotropism. This approach can be applied to any fluorescently labeled target in the brain.

Introduction:

45

46   Virus species from multiple virus families are neuroinvasive and neurotropic [1,2] . These viruses

47   not only cross the physical brain barriers, but also infect the central nervous system, potentially

48   leading to lethal encephalitis or long-term neurological sequelae among survivors [3-5]. While global

49   disease burden remains high, better understanding of viral pathogenesis is required for the

50   development of effective diagnosis, therapy, and prevention measures [6,7]. One of the major

51   obstacles for studying viral pathogenesis within the entire brain is the lack of feasible imaging

52   approaches to visualize virus infection at cellular to subcellular levels, while still providing a

53   global view within a preserved anatomical tissue context.

54   While confocal microscopy provides invaluable information at the subcellular level, any three-

55   dimensional (3D) information provided by the approach is limited to the μm–mm range. Since

56   neurons consist of cell bodies with long axons that can project to distant brain areas, it is extremely

57   challenging to obtain an overall view of viral distribution within the context of the entire brain

58   based solely on tissue section analyses. Mesoscopic techniques such as optical projection

59   tomography (OPT) and light sheet fluorescence microscopy (LSFM) are 3D imaging techniques

60   for transparent mesoscopic sized (mm- a few cm) tissue samples; and therefore, are suitable for

61   whole rodent brain imaging. These methods can provide information at cellular resolution while

62   still capturing the entire tissue in 3D and have been used in various applications for targeted

63   imaging, such as, whole organ distribution of specific protein expression via immunolabeling [8-10].

64   However, anatomical information obtained from OPT, based on tissue autofluorescence, is limited.

65   Magnetic resonance imaging (MRI), conversely, is widely used for anatomical brain imaging since

66   it has exquisite contrast and resolution [11]. In its turn, structural MRI is not suitable for imaging

67   pathogens.

68   For a holistic view of viral brain infection, here, we devised an imaging approach that, for the first

69   time, provides spatial distribution of virus infection in the brain, with precise anatomical mapping.

70   Specifically, we generated an MRI template for *ex vivo* optically cleared adult mouse brains and

71   coregistered it with whole brain viral signal acquired from 3D OPT images ($\sim$0.5 cm^3). We used

72   this approach to evaluate, the detailed distribution of Langat virus (LGTV), a model neurotropic

73   flavivirus, in wild type (WT) mice and mice lacking type I interferon (IFN) response, *Ifnar*$^{-/-}$. Type

74   I IFN response is the first line of antiviral defense in the brain and can, therefore, influence viral

75   distribution [12]. In conjunction with confocal and electron microscopy, which confirmed the

76   presence of virus infection in the identified areas, we can also identify the cellular tropism of virus

77   infection in the brain. The developed MRI template and MRI-OPT coregistration approach enable

78   precise anatomical mapping of any signal obtained from *ex vivo* optical brain images. It is an

79   invaluable tool to study whole brain viral distribution with precise anatomical context and is

80   applicable for any pathogen.

81

82   **Results:**

83   ***Whole brain 3D imaging of virus infection***

84   Previous studies have confirmed LGTV infection in rodent brains using immunohistochemistry or

85   quantitative PCR [13-15]. However, the complete overview of viral distribution throughout the whole

86   brain is still unknown. Therefore, we first established an approach for imaging virus infection in

87   the whole brain and tested its biological value using WT and *Ifnar*$^{-/-}$mice. We infected the mice

88   with LGTV, immunolabeled the brains against LGTV nonstructural protein 5 (NS5), optically

89   cleared and scanned the brains with OPT. This novel approach allowed visualization of virus

4

90 infection throughout the whole brain. We observed that $Ifnar^{-/-}$ mice were more susceptible for

91 infection (Supplementary Fig. 1) and that viral distribution in these mice was strikingly different

92 when compared to WT mice (Fig. 1a, Supplementary Fig. 2, Supplementary Movie 1). In $Ifnar^{-/-}$

93 brains, we observed pronounced infection, spanning from the interior wall of the lateral ventricles

94 to the anterior cerebrum and olfactory bulbs, resembling the rostral migratory stream, in addition

95 to third ventricle and fourth ventricle choroid plexus (ChP). To complement OPT data, we used

96 LSFM to visualize fourth ventricle ChP infection at high resolution (Supplementary Movie 2). We

97 also observed weak infection in the cerebral cortex compared to other areas. By contrast, in WT

98 mice, infection was mainly localized in cerebral cortex, with no detectable infection in rostral

99 migratory stream, lateral ventricle, and fourth ventricle (Fig. 1a, Supplementary Fig. 2, and

100 Supplementary Movie 1). Of note, we also detected some low-level unspecific signal in uninfected

101 brains (mock group) (Fig. 1a and Supplementary Fig. 2), most likely due to ventricular antibody

102 trapping or unspecific antibody absorption in meninges during whole brain immunolabeling.

103 In theory, OPT or LSFM imaging allows for the study of any immunolabeled pathogen or protein

104 of choice. However, it greatly depends on the availability of specific antibodies that can withstand

105 harsh chemical treatment and their ability to penetrate the brain. Detection of an endogenously

106 expressed fluorescent protein could bypass the need for these specific antibodies. Several GFP-

107 expressing pathogens already exist; however, several fluorescent proteins, especially green

108 fluorescent protein (GFP), are severely quenched during the clearing process [10]. Therefore, we

109 investigated whether an anti-GFP antibody could be used as a general OPT probe. Accordingly,

110 we infected $Ifnar^{-/-}$ mice with GFP-expressing LGTV (LGTV-GFP) and immunolabeled the brain

111 $ex\ vivo$ with anti-NS5 and anti-GFP antibodies. We observed a clear overlap between OPT signals

112 from viral NS5 and GFP-expressing virus, indicating the possibility to visualize any GFP-

5

113   expressing pathogen in the brain using OPT without the need of specific antigens (Fig. 1b,

114   Supplementary Movie 3). Taken together, we were able to visualize viral infection and viral

115   distribution in the whole brain using 3D imaging. Furthermore, our 3D OPT approach can be

116   translated to study whole brain distribution of any GFP- labeled pathogen.

117

118   ***OPT-MRI coregistration for anatomical mapping of virus infection***

119   We have now shown that OPT allows visualization of viral brain infection with great sensitivity

120   and high spatial resolution. However, the anatomical information obtained from tissue

121   autofluorescence is insufficient to provide a detailed anatomical reference frame for the multitude

122   of structures the brain can be divided in [16] and which are involved in different physiological

123   functions. Therefore, we are in need of an improved anatomical reference frame, allowing precise

124   identification of the infected brain areas.

125   To address this, we coregistered our viral OPT images with structural MR images. Because our

126   OPT images are acquired *ex vivo* after extensive chemical tissue processing, we acquired *ex vivo*

127   MR images after chemical preprocessing and OPT acquisition (Fig. 2a). We then coregistered

128   these MR images with viral OPT signal, which resulted in fusion images with good spatial

129   alignment (Fig. 2b). To obtain an anatomical reference with improved anatomical detail and tissue

130   contrast and to overcome high MR-scanning costs of individual brains in the future, we created a

131   high-resolution *ex vivo* MRI brain template, acquired after tissue bleaching and clearing for optical

132   imaging. We designed a novel study- and sequence specific brain template by serial longitudinal

133   registration of ten optically cleared brains and generated corresponding tissue probability maps

134   (TPMs) (Fig. 2 c-e), required for image segmentation and image normalization (warping) to the

135   template, as described in the Materials and methods. Afterwards, we created a study-specific

136   animal preset in the toolbox SPMMouse (http://spmmouse.org) [17], which resulted in improved

137   warping and normalization of viral OPT signal to the template. Finally, we normalized individual

138   differences in tissue deformation to compensate for natural variation in brain size, which allowed

139   for improved coregistration of viral signal, mainly in the olfactory bulbs. In optimized OPT-MRI

140   template fusion images, the viral signal was displayed within a detailed anatomical context

141   provided by MRI (Fig. 2d,f), allowing for precise identification of infected brain regions.

142   ***Highly accurate brain map of viral infection***

143   The OPT images displaying viral signal in the whole brain together with the study-specific brain

144   template, provide a detailed anatomical reference frame after coregistration. This allowed us to

145   proceed to our ultimate goal, namely, to evaluate the differential viral distribution patterns in WT

146   and *Ifnar*$^{-/-}$ mice (Fig. 3). The high-resolution viral signal displayed within the detailed anatomy,

147   afforded by OPT-MRI coregistration offered unprecedented detail and insights into viral brain

148   distribution. In *Ifnar*$^{-/-}$ mice, we detected specific infection in grey matter (GM), white matter

149   (WM), and the ventricular system (Fig. 3a-c, left panels). For GM, we observed viral signal in the

150   granular cell layer of the olfactory bulb, entorhinal cortex, dorsal endopiriform nucleus, piriform

151   area, agranular insula, primary visual field, and primary somatosensory cortex (upper limb and

152   barrel field). In WM, we detected viral signal in the olfactory limb of the anterior commissure,

153   anterior forceps of corpus callosum, and supra-callosal WM. The identified regions are part of

154   distinct sensory systems, such as the olfactory system, visual system, and somatosensory system.

155   We also observed viral signal in ChP and the interior wall of lateral ventricles, third ventricle, and

156   fourth ventricle. Of note, ChP of the lateral ventricle, subventricular zone, and the olfactory limb

157   of the anterior commissure are all parts of the rostral migratory stream, suggesting specific

7

158   infection of the ventriculo–olfactory neurogenic system by LGTV. In WT mice, however, the viral

159   signal was limited to entorhinal cortex, piriform area, primary visual field and the third ventricle

160   (Fig. 3a-c, right panels), suggesting a major influence of the type I IFN response on virus

161   infectivity and distribution in the mouse brain.

162   *Validation of OPT-MRI viral signals by confocal and electron microscopy*

163   Guided by OPT-MRI fusion images, we confirmed LGTV infection in the brain regions identified

164   as infected in whole brain imaging on sections using confocal and electron microscopy. Apart from

165   confirming the presence of viral infection in these areas, it also allowed us to investigate viral

166   cellular tropism, leading to new biological insights. In rostral migratory stream, we observed viral

167   infection in immature neurons in both mouse models (Fig. 4a). However, we only observed viral

168   infection in leptomeninges, endothelial cells lining the blood vessels in the subarachnoid space,

169   ChP epithelial cells and ependymal cells lining the ventricular wall in $Ifnar^{-/-}$ but not WT brains

170   (Fig. 4b-c and Supplementary Fig. 3a,b). This result confirms that the signal observed from these

171   areas in the OPT images of LGTV infected and mock WT brains was due to non-specific antibody

172   absorption (Fig. 1a and Supplementary Fig. 2). To further confirm the presence of virus, we imaged

173   fourth ventricle ChP of $Ifnar^{-/-}$ brain, identified as highly infected on OPT-MRI, using electron

174   microscopy. Transmission electron microscopy (TEM) imaging of ChP epithelial cells, marked by

175   the presence of cilia, revealed extreme distortion of endoplasmic reticulum (ER) membranes in the

176   infected compared to mock tissue (Fig. 4d and Supplementary Fig. S3c,d). High-magnification

177   analysis revealed virus particles in the ER lumen (Fig. 4d, inset a) and the formation of viral

178   replication complexes, as bud-like invaginations of the ER membrane (Fig. 4d, inset ii).

179   Segmentation of volume images taken by focused ion beam milling-scanning electron microscopy

180   (FIB-SEM) showed the 3D architecture of replication complexes within ER of infected cells (Fig.

8

181   4e-f, Supplementary Fig. 3e and Supplementary Movie 4). Lastly, we investigated infection in

182   cerebral cortex, focusing on the piriform area and entorhinal cortex. In both mouse models, we did

183   not observe infection in astrocytes (Supplementary Fig. 3f). However, we observed infection in

184   mature neurons in WT brain, while microglia remained uninfected (Fig. 4g). Surprisingly, we

185   observed the opposite cellular tropism in *Ifnar*$^{-/-}$brains, namely infected microglia and refractory

186   neurons, (Fig. 4g), indicating that the type I IFN response shapes cellular tropism of viral infection

187   in the brain. Taken together, our OPT-MR fusion technique allowed us to specifically identify

188   infected regions, which could then be used to further investigate viral behavior in more detail,

189   leading to the discovery of this remarkable tropism shift under influence of the type 1 IFN

190   response.

191

192   **Discussion:**

193   Imaging techniques provide pivotal information on biological processes in cells and tissues. Each

194   technique has its own advantages and limitations, such as spatial resolution and specimen size,

195   which makes it challenging to observe detailed biological phenomena while maintaining an

196   overview of the whole organ and its anatomical reference frame. Here, we report a whole brain

197   imaging approach, which allows visualization of fluorescent targeted signals from OPT and precise

198   anatomical brain mapping when applied in combination with our developed MR template for

199   optically cleared brains. This allowed subsequent targeting of brain regions for higher-resolution

200   imaging using confocal and 3D electron microscopy. The novel approach can be utilized as a tool

201   to improve our understanding of viral pathogenesis or, in fact, of any immunolabeled target, in the

202   whole mouse brain.

203   Considering the mesoscopic sample size (mm-cm) and the reasonable scan times (~ 90 min per

204   brain) to obtain high-resolution (13.2 µm for our setting), OPT seems ideally suited to visualize

205   viral distribution in the whole mouse brain. However, since OPT systems are not commercially

206   available, LSFM is often applied. Our approach could also be applied to LSFM to visualize viral

207   distribution in the whole brain with even higher resolutions as compared to OPT but with

208   consequent elongated scanning times. One should also keep in mind that, in contrast to OPT and

209   MRI, LSFM results in images with non-isotropic voxels, leading to slight mismatch alignment of

210   LSFM-MR fusion images.

211   To date, various mouse brain templates that can be used as an anatomical reference are available.

212   However, they are either based on histology [16,18] or, *in vivo* or *ex vivo in situ* MRI [19-21]. However,

213   OPT images are acquired *ex vivo* after bleaching and optical clearing. These chemical treatments

214   result in a certain level of tissue alteration, which lead to misalignment when coregistering brain

215   OPT signals to these existing templates. Therefore, we designed a study-specific brain template

216   consisting of *ex vivo* MR scans, acquired after OPT pre-processing, and coregistered it with viral

217   OPT signal, which yielded exact alignment and allowed precise identification of infected brain

218   regions. It should be noted here, however, that the template is based on brains that underwent

219   particular chemical permeabilization and bleaching and, that were cleared with BABB (see

220   Materials and methods). The application of distinct pre-processing and clearing protocols, such as

221   iDisco [22], may affect the brain differently and lead to divergent brain deformations.

222   In this study, we also showed that OPT-MRI coregistration set the base for novel insights in

223   infection biology. The fusion images revealed distinct infection patterns driven by type I IFN

224   response. In *Ifnar*^{−/−} mice, infection mainly localized in regions belonging to the visual,

225   somatosensory, and, most extensively, olfactory system, while in WT infection was mainly

10

226   restricted to regions processing olfactory information, which have been previously reported for

227   other flaviviruses [23,24]. The susceptibility of the olfactory system to LGTV infection in both WT

228   and *Ifnar*^{−/−}brains implies that the type I IFN response is, in itself, not sufficient to protect this

229   neuronal circuit from viral infection. In contrast, the susceptibility of the ChP and leptomeninges,

230   which were only permissive to viral infection in *Ifnar*^{−/−}brains, indicates that the antiviral

231   properties of these tissues greatly depend on type I IFN response. Lastly, while infection in *Ifnar*[−]

232   [/−]brains could be found in both WM and GM, infection in WT brains was restricted to the latter.

233   This restriction might, at least in part, relate to the surprising cellular tropism shift from mature

234   neurons in WT to microglia in *Ifnar*^{−/−}brains (Fig. 4g). In WT, the virus infected the cell body of

235   mature neurons, residing in GM, while in *Ifnar*^{−/−}, the virus infected microglia, which reside both

236   in GM and WM. To the best of our knowledge, such striking cellular tropism shift has not been

237   reported to date *in vitro* or *in vivo.*

238   Collectively, we demonstrate that OPT-MRI fusion images enable precise whole brain mapping

239   of viral 3D fluorescence signal and, that the creation of such images opens the door to novel

240   insights in infection biology. Since the approach is not only applicable to image viral infection but

241   can be translated to any fluorescently labeled target in the brain, visualized by OPT or LSFM, it

242   holds the power to improve our knowledge and understanding of any neurological condition with

243   anatomical precision.

244

245   **Materials and Methods:**

246   *Animals*

247   C57BL/6 WT mice and interferon alpha receptor knockout (*Ifnar*^{−/−}) mice in C57BL/6 background

248   were kindly provided by N.O. Gekara (Department of Molecular Biology, Umeå University;

11

249   current address: Department of Molecular Biosciences, The Wenner-Gren Institute, Stockholm

250   University, Sweden) [12]. Mice were bred as homozygotes and maintained under specific pathogen-

251   free conditions. All animal experiments were conducted at the Umeå Centre for Comparative

252   Biology (UCCB). All animal experiments were approved by the regional Animal Research Ethics

253   Committee of Northern Norrland and by the Swedish Board of Agriculture (ethical permits: A9-

254   2018 and A41-2019), and all procedures were performed according to their guidelines.

255

256   *Viruses*

257   LGTV strain TP21 was a kind gift from G. Dobler (Bundeswehr Institute of Microbiology,

258   Munich, Germany) and GFP-expressing LGTV (LGTV-GFP) infectious clone was a kind gift from

259   A. Pletnev (NIAID, NIH) [25]. LGTV stock was produced in VeroB4 cells, a kind gift from G.

260   Dobler, [26] and harvested on day 3 post infection when cytopathic effect was apparent. A 1:1

261   mixture of VeroB4 and HEK 293T cells, a kind gift from F. Weber (Biomedical Research Center

262   Seltersberg (BFS), Justus Liebig University Giessen, Germany) was transfected with the LGTV-

263   GFP plasmid using GeneJuice® Transfection Reagent (#70967, Sigma Aldrich, USA), following

264   manufacturer's protocol. Virus supernatant was harvested on day 7 post infection. Both virus

265   stocks were titrated on VeroB4 cells using focus-forming assay [26].

266

267   *Virus infection in mouse model*

268   For the experiments, the animals (7- to 11-week-old, mixed gender) were randomly divided into

269   the following groups: WT, mock-infected; WT, LGTV-infected; *Ifnar*$^{-/-}$, LGTV-infected. After

270   sedation with ketamine (100 µg/g body weight) and xylazine (5 µg/g body weight), the animals

271   were intracranially inoculated with 1000 pfu of LGTV or with 10,000 pfu of LGTV-GFP

12

272 suspended in 20 μL of PBS. Infected mice were euthanized using O_2 deprivation when they

273 developed any one severe symptom, such as: >20% weight loss, bilateral eye infection, diarrhea,

274 or hind-limb paralysis; or when they developed three milder symptoms, such as: >15% weight

275 loss, unilateral eye infection, facial edema, ruffled fur, or overt bradykinesia, and/or development

276 of stereotypies. Following euthanasia, cardiac perfusion was performed using 20 mL of PBS,

277 followed by 20 mL of 4% w/v paraformaldehyde (PFA) in PBS, after which the perfused brain

278 was removed for *ex vivo* analysis.

279

280 ***Whole-mount immunohistochemistry (IHC) and OPT***

281 PFA-fixed brain was fluorescently immunolabeled with an antibody against viral NS5

282 (Supplementary Table 1) and processed for OPT imaging, as previously described [27,28]. Briefly,

283 the brain was dehydrated in a stepwise gradient of methanol (MeOH), permeabilized by repeated

284 freeze–thawing in MeOH at –80 °C and a bleaching solution (MeOH:H_2O_2:DMSO at 2:3:1) to

285 quench tissue autofluorescence. For immunolabeling, specimens were rehydrated in TBST (50

286 mM Tris-HCl, pH 7.4, 150 mM NaCl, and 0.1% v/v TritonX-100), blocked with 10% v/v normal

287 goat serum (NGS) (#CL1200-100, Nordic Biosite, Sweden), 5% v/v DMSO, and 0.01% w/v

288 sodium azide in TBST at 37 °C for 48 h, and labeled with primary (chicken anti-NS5 and/or rabbit

289 anti-GFP, Supplementary Table 1) and secondary (goat anti-chicken Alexa Fluor 680 and/or

290 donkey anti-rabbit Alexa Fluor 594, Supplementary Table 1) antibodies diluted in blocking buffer.

291 They were incubated at 37 °C for 4 d at each staining step. The stained tissue was mounted in 1.5%

292 w/v low melting point SeaPlaque™ agarose (#50101, Lonza, Switzerland) and optically cleared

293 using a BABB solution (benzyl alcohol (#1.09626.1000, Supelco, USA) : benzyl benzoate

294 (#10654752, Thermo Fisher Scientific, USA) at 1:2).

13

295 OPT imaging was performed with an in-house developed near-infrared OPT (NIR-OPT) system

296 described in detail in Eriksson et al. [28], with a zoom factor of 1.6 or 2.0, that resulted in an isotropic

297 voxel dimension of 16.5 μm^3 and 13.2 μm^3, respectively. To obtain specific fluorescent viral (NS5)

298 signal coupled with Alexa Fluor 680, anti-GFP antibody coupled with Alexa Fluor 594, and tissue

299 autofluorescence signals, OPT images were acquired at the following filter settings: Ex: 665/45

300 nm, Em: 725/50 nm (exposure time: 7000 ms); Ex: HQ565/30, Em: 620/60 (exposure time: 5000

301 ms); and Ex: 425/60 nm, Em: 480 nm (exposure time: 500 ms), respectively.

302 To increase the signal-to-noise ratio for NS5, the pixel intensity range of all images was adjusted

303 to display the minimum and maximum, and a contrast-limited adaptive histogram equalization

304 (CLAHE) algorithm with a tile size of 64 × 64 was applied to projection images acquired in the

305 NS5 channel [29]. Tomographic reconstruction was performed using NRecon software (v.1.7.0.4,

306 Skyscan microCT, Bruker, Belgium) with additional misalignment compensation and ring artifact

307 reduction. Image files were converted to Imaris files (.ims) using the Imaris file converter (v9.5.1,

308 Bitplane, UK). NS5 signal from all imaged brains was adjusted to display at min = 0, max = 200,

309 and gamma = 1.2, and colored using red glow color scheme. The signal was superimposed onto

310 the corresponding tissue autofluorescence image using 3D iso-surface rendering in Imaris software

311 (v9.5.1, Bitplane).

312

313 *Light sheet fluorescent imaging*

314 High-resolution images of ChP in the fourth ventricle of individual *Ifnar*$^{-/-}$ brains, previously

315 scanned using OPT, were acquired by LSFM. To compensate for any phototoxic effects on

316 immunofluorescence from homogeneous sample illumination during OPT acquisition, the sample

317 was relabeled using both primary and secondary antibodies (see above) and cleared in BABB

14

318 without agarose mounting. The brain was then scanned using an UltraMicroscope II (Miltenyi

319 Biotec, Germany) with a 1× Olympus objective (PLAPO 2XC, Olympus, Japan), coupled to an

320 Olympus zoom body providing 0.63–6.3× magnification with a lens-corrected dipping cap

321 MVPLAPO 2× DC DBE objective (Olympus). For image acquisition, left and right light sheets

322 were merged with a 0.14 numerical aperture, which resulted in a light sheet z-thickness of 3.87 μm

323 and 60% width, while using a 10–15 step blending dynamic focus across the field of view. Image

324 sections were generated by Imspector Pro software (v7.0124.0, LaVision Biotec Gmbh, Germany)

325 and stitched together using the TeraStitcher script (v9), implemented in Imspector Pro. Stitched

326 images were then converted into Imaris files (*.ims files) using the Imaris file converter (v9.5.1,

327 Bitplane).

328

329 *MRI acquisition*

330 After OPT or LSFM imaging, 10 brains were rehydrated in TBST. T1-weighted images were then

331 acquired at 9.4 Tesla using a preclinical MR system (Bruker BioSpec 94/20, Bruker, Germany)

332 equipped with a cryogenic RF coil (MRI CryoProbe, Bruker) running Paravision 7.0 software

333 (Bruker). Specifically, Modified Driven Equilibrium Fourier Transform (MDEFT) sequence with

334 5 repetitions (TR: 3000 ms; TE: 3 ms; TI: 950 ms; voxel dimension: $40 \times 40 \times 40mm^3$) was

335 performed. Postprocessing of images involved the realignment and averaging of individual

336 repetitions using statistical parametric mapping (SPM8) (the Wellcome Trust Centre for

337 Neuroimaging, UCL, UK; www.fil.ion.ucl.ac.uk/spm) implemented in Matlab (R2014a, The

338 MathWorks Inc., USA).

339

340 *MRI template creation*

15

341 A study-specific MRI template was created using bias-corrected (SPM8) MR images (n = 10),

342 which were realigned and averaged using serial longitudinal registration in SPM12 implemented

343 in Matlab (R2015b, The MathWorks Inc.). Then, all individual MR scans were coregistered with

344 the template image. Study- and sequence-specific segments and TPMs were created using a 2-step

345 segmentation and DARTEL pipeline initially based on in-house generated tissue priors. Briefly, a

346 primary segmentation and DARTEL algorithm was applied to individual T1-weighted images to

347 generate preliminary tissue priors for the study, using the toolbox SPMmouse. The entire process

348 was then repeated (segmentation + DARTEL) using the tissue priors generated at the first step to

349 produce study- and sequence-specific TPMs.

350

351 ***Creation of OPT-MRI fusion images***

352 OPT images with viral signal and autofluorescence signal were reconstructed in DICOM format

353 using NRecon software (v.1.7.0.4, Bruker) followed by their conversion into NifTi using PMOD

354 VIEW tool (v.4.2, PMOD Technologies Inc., Switzerland) or the dcm2nii tool in MRIcron

355 software for OPT and MR images, respectively. Coregistration of OPT with the study-specific

356 MRI template was performed using the toolbox SPMmouse in SPM8. Voxel-to-voxel affine

357 transformation matrices were calculated using individual tissue autofluorescence from OPT

358 images and applied to the corresponding viral OPT images. Fusion images of viral OPT signal

359 were created for each individual brain using its own MRI and with the study-specific MRI template

360 using the PMOD VIEW tool or Amira-Avizo software (v6.3.0, Thermo Fisher Scientific) for 3D

361 renderings. Finally, brain areas with viral signal were identified according to the Turone Mouse

362 Brain Template and Atlas (TMBTA) [21].

363

364 *IHC for brain slice*

365 PFA-fixed brain was washed in PBS, dehydrated overnight in a 30% w/v sucrose solution, snap-

366 frozen on dry ice in Optimal Cutting Temperature medium (#361603E, VWR, USA), and stored

367 at –80 °C until cryosectioning. The organ was sectioned along the sagittal plane at 10 μm thickness

368 using a rotatory microtome cryostat (Microm Microtome Cryostat HM 500M, Microm, USA).

369 Brain sections were permeabilized and blocked in 10% v/v NGS, 0.2% v/v TritonX-100, an 1%

370 w/v bovine serum albumin in PBS for 1 h at room temperature (RT), immunolabelled with primary

371 antibodies overnight at 4 °C, and then labeled with fluorescent secondary antibody for 1 h at RT

372 in the dark. For immunodetection, the primary and secondary antibodies (Supplementary Table 1)

373 were diluted in 2% v/v NGS and 0.5% v/v TritonX-100 in PBS. Confocal fluorescence microscopy

374 was performed using a Zeiss 710 confocal microscope (Zeiss, Germany) controlled by Zeiss Zen

375 interface (v.14.0.19.201) with Axio Observer inverted microscope equipped with Plan

376 Apochromat 20×/0.8, C-Apochromat 40×/1.2, and Plan Apochromat 63×/1.4 objective lens.

377 Large-area imaging was performed using a Nikon Eclipse Ti-E inverted microscope (Nikon,

378 Japan) with an DU897 ANDOR EMCCD camera controlled by Nikon NIS Elements interface,

379 equipped with Nikon CFI Plan Apochromat 10× (N.A. 0.45) DIC objective. To portray the large

380 area, composite images were created by stitching together individual images using NIS-Elements

381 AR software (v5.21.03, Nikon).

382

383 *Fixation, resin embedding, and staining of tissue for electron microscopy*

384 ChP from the brain of LGTV-infected *Ifnar*$^{-/-}$ mice were prepared for electron microscopy by

385 cardiac perfusion with 20 mL of 0.1 M phosphate buffer, followed by 20 mL of 2.5% w/v

386 glutaraldehyde and 4% w/v PFA in 0.1 M phosphate fixative solution. Fourth ventricle ChP was

387   dissected and further immersed in the same fixative solution for an additional 24 h. The tissue was

388   stained and subsequently embedded in resin using the rOTO (reduced osmium tetroxide,

389   thiocarbohydrazide, osmium tetroxide) method [30]. The tissue samples were placed in a solution of

390   1.5% w/v potassium ferrocyanide and 2% w/v osmium tetroxide (OsO_4), and then incubated in

391   Pelco Biowave Pro+ (Pelco, Fresno, USA), a microwave tissue processor ("the processor"), under

392   vacuum for 14 min. After two rinses with MilliQ water on the bench, the samples were washed

393   twice with MilliQ water in the processor without vacuum pressurization. Then, the samples were

394   incubated in 1% w/v thiocarbohydrazide solution for 20 min. After another MilliQ water rinse on

395   the bench, the samples were again washed twice in the processor (no vacuum). Next, the samples

396   were placed in 2% w/v OsO_4 solution and run in the processor under vacuum for 14 min, followed

397   by an additional water and processor wash. The samples were placed in 1% w/v uranyl acetate

398   solution and run in the processor under vacuum for 12 min, followed by another water and

399   processor wash. The samples were then dehydrated in an ethanol gradient series, by removing and

400   adding ethanol solutions of increasing concentrations (each step was performed in processor,

401   without vacuum pressurization): 30%, 50%, 70%, 80%, 90%, 95%, and 100% (twice). The

402   dehydrated samples were infiltrated with an increasing concentration of Durcupan ACM resin

403   (Sigma-Aldrich) using the following stepwise ratios of ethanol to Durcupan resin: 1:3, 1:1, and

404   3:1. All steps were performed in the processor for 3 min under vacuum. The two final infiltration

405   steps were performed in 100% resin. Finally, the samples were transferred to tissue molds, and

406   placed at 60 °C for 48 h for complete polymerization of the resin.

407

408   ***TEM***

409 Using a Reichert UltraCut S ultramicrotome (Leica, Germany), resin-embedded samples were

410 trimmed, and 50 nm sections were cut using a diamond knife and placed onto copper slot grids.

411 Resin-embedded sections were imaged using a 120 kV Talos L120C transmission electron

412 microscope (Thermo Fischer Scientific) fitted with a LaB6 filament and Ceta 4k × 4k CMOS

413 camera sensor. Images were acquired at 2600×, 8500×, and 36,000× magnification corresponding

414 to a pixel size of 54.3, 17.0, and 4.1 Å/px, respectively, at the specimen level. TEM images were

415 analyzed by ImageJ software (NIH).

416

417 *Volume imaging using FIB-SEM*

418 Resin-embedded tissue blocks were trimmed, mounted on SEM stubs, and then coated with a 5

419 nm platinum layer using a Q150T-ES sputter coater (Quorum Technologies, UK) before FIB-SEM

420 volume imaging. Data was acquired using Scios Dual beam microscope (FIB-SEM) (Thermo

421 Fischer Scientific). Electron beam imaging was acquired at 2 kV, 0.1 nA current, 1.9 × 1.9 nm

422 pixel spacing, 7 mm working distance, 10 μs acquisition time, and 3072 × 2048 resolution using a

423 T1 detector. SEM images were acquired every 20 nm. The working voltage of gallium ion beam

424 was set at 30 kV, and 0.5 nA current was used for FIB milling. The specimens were imaged at 5 ×

425 5 μm block face and 5 μm depth. FIB milling and SEM imaging were automated using the Auto

426 Slice and View software (Thermo Fischer Scientific). SEM volume images were aligned and

427 reconstructed using ImageJ (NIH) with linear stack alignment, with SIFT and

428 MultiStackRegistration plugins [31,32]. Analysis and segmentation of SEM volume images was done

429 using Amira-Avizo software (v2020.3.1, Thermo Fisher Scientific).

430

431 **Data availability:**

432   All data are available in the main text or the supplementary materials. MR template will be

433   deposited at NeuroImaging Tools and Resources Collaboratory (NITRC) and publicly available

434   upon publication of the manuscript.

435

436   **References:**

437   1   Sips, G. J., Wilschut, J. & Smit, J. M. Neuroinvasive flavivirus infections. *Rev Med Virol*

438   22, 69-87, doi:10.1002/rmv.712 (2012).

439   2   Gosztonyi, G. & Koprowski, H. The concept of neurotropism and selective vulnerability

440   ("pathoclisis") in virus infections of the nervous system--a historical overview. *Curr Top*

441   *Microbiol Immunol* 253, 1-13, doi:10.1007/978-3-662-10356-2_1 (2001).

442   3   Sejvar, J. J. The long-term outcomes of human West Nile virus infection. *Clin Infect Dis*

443   44, 1617-1624, doi:10.1086/518281 (2007).

444   4   Turtle, L., Griffiths, M. J. & Solomon, T. Encephalitis caused by flaviviruses. *QJM* 105,

445   219-223, doi:10.1093/qjmed/hcs013 (2012).

446   5   Gould, E. A. & Solomon, T. Pathogenic flaviviruses. *Lancet* 371, 500-509,

447   doi:10.1016/S0140-6736(08)60238-X (2008).

448   6   Ruzek, D. *et al.* Tick-borne encephalitis in Europe and Russia: Review of pathogenesis,

449   clinical features, therapy, and vaccines. *Antiviral Res* 164, 23-51,

450   doi:10.1016/j.antiviral.2019.01.014 (2019).

451   7   Kubinski, M. *et al.* Tick-Borne Encephalitis Virus: A Quest for Better Vaccines against a

452   Virus on the Rise. *Vaccines (Basel)* 8, doi:10.3390/vaccines8030451 (2020).

453 8   Alanentalo, T. *et al.* Quantification and three-dimensional imaging of the insulitis-
454   induced destruction of beta-cells in murine type 1 diabetes. *Diabetes* 59, 1756-1764,
455   doi:10.2337/db09-1400 (2010).

456 9   Sharpe, J. *et al.* Optical projection tomography as a tool for 3D microscopy and gene
457   expression studies. *Science* 296, 541-545, doi:10.1126/science.1068206 (2002).

458 10 Dodt, H. U. *et al.* Ultramicroscopy: three-dimensional visualization of neuronal networks
459   in the whole mouse brain. *Nat Methods* 4, 331-336, doi:10.1038/nmeth1036 (2007).

460 11 Bocan, T. M., Panchal, R. G. & Bavari, S. Applications of in vivo imaging in the
461   evaluation of the pathophysiology of viral and bacterial infections and in development of
462   countermeasures to BSL3/4 pathogens. *Mol Imaging Biol* 17, 4-17, doi:10.1007/s11307-
463   014-0759-7 (2015).

464 12 Muller, U. *et al.* Functional role of type I and type II interferons in antiviral defense.
465   *Science* 264, 1918-1921, doi:10.1126/science.8009221 (1994).

466 13 Weber, E. *et al.* Type I interferon protects mice from fatal neurotropic infection with
467   Langat virus by systemic and local antiviral responses. *J Virol* 88, 12202-12212,
468   doi:10.1128/JVI.01215-14 (2014).

469 14 Kurhade, C. *et al.* Type I Interferon response in olfactory bulb, the site of tick-borne
470   flavivirus accumulation, is primarily regulated by IPS-1. *J Neuroinflammation* 13, 22,
471   doi:10.1186/s12974-016-0487-9 (2016).

472 15 Maffioli, C., Grandgirard, D., Engler, O. & Leib, S. L. A tick-borne encephalitis model in
473   infant rats infected with langat virus. *J Neuropathol Exp Neurol* 73, 1107-1115,
474   doi:10.1097/NEN.0000000000000131 (2014).

475 16 Wang, Q. *et al.* The Allen Mouse Brain Common Coordinate Framework: A 3D

476   Reference Atlas. *Cell* 181, 936-953 e920, doi:10.1016/j.cell.2020.04.007 (2020).

477 17 Sawiak, S. J., Wood, N. I., Williams, G. B., Morton, A. J. & Carpenter, T. A. Voxel-

478   based morphometry with templates and validation in a mouse model of Huntington's

479   disease. *Magn Reson Imaging* 31, 1522-1531, doi:10.1016/j.mri.2013.06.001 (2013).

480 18 Sunkin, S. M. *et al.* Allen Brain Atlas: an integrated spatio-temporal portal for exploring

481   the central nervous system. *Nucleic Acids Res* 41, D996-D1008, doi:10.1093/nar/gks1042

482   (2013).

483 19 Hikishima, K. *et al.* In vivo microscopic voxel-based morphometry with a brain template

484   to characterize strain-specific structures in the mouse brain. *Sci Rep* 7, 85,

485   doi:10.1038/s41598-017-00148-1 (2017).

486 20 Dorr, A. E., Lerch, J. P., Spring, S., Kabani, N. & Henkelman, R. M. High resolution

487   three-dimensional brain atlas using an average magnetic resonance image of 40 adult

488   C57Bl/6J mice. *Neuroimage* 42, 60-69, doi:10.1016/j.neuroimage.2008.03.037 (2008).

489 21 Barriere, D. A. *et al.* Brain orchestration of pregnancy and maternal behavior in mice: A

490   longitudinal morphometric study. *Neuroimage* 230, 117776,

491   doi:10.1016/j.neuroimage.2021.117776 (2021).

492 22 Renier, N. *et al.* iDISCO: a simple, rapid method to immunolabel large tissue samples for

493   volume imaging. *Cell* 159, 896-910, doi:10.1016/j.cell.2014.10.010 (2014).

494 23 Stadtbaumer, K., Leschnik, M. W. & Nell, B. Tick-borne encephalitis virus as a possible

495   cause of optic neuritis in a dog. *Vet Ophthalmol* 7, 271-277, doi:10.1111/j.1463-

496   5224.2004.04030.x (2004).

497 24 Fu, T. L., Ong, K. C., Tan, S. H. & Wong, K. T. Japanese Encephalitis Virus Infects the

498   Thalamus Early Followed by Sensory-Associated Cortex and Other Parts of the Central

499   and Peripheral Nervous Systems. *J Neuropathol Exp Neurol* 78, 1160-1170,

500   doi:10.1093/jnen/nlz103 (2019).

501 25 Grabowski, J. M. *et al.* Flavivirus Infection of Ixodes scapularis (Black-Legged Tick) Ex

502   Vivo Organotypic Cultures and Applications for Disease Control. *mBio* 8,

503   doi:10.1128/mBio.01255-17 (2017).

504 26 Overby, A. K., Popov, V. L., Niedrig, M. & Weber, F. Tick-borne encephalitis virus

505   delays interferon induction and hides its double-stranded RNA in intracellular membrane

506   vesicles. *J Virol* 84, 8470-8483, doi:10.1128/JVI.00176-10 (2010).

507 27 Alanentalo, T. *et al.* Tomographic molecular imaging and 3D quantification within adult

508   mouse organs. *Nat Methods* 4, 31-33, doi:10.1038/nmeth985 (2007).

509 28 Eriksson, A. U. *et al.* Near infrared optical projection tomography for assessments of

510   beta-cell mass distribution in diabetes research. *J Vis Exp*, e50238, doi:10.3791/50238

511   (2013).

512 29 Hornblad, A., Cheddad, A. & Ahlgren, U. An improved protocol for optical projection

513   tomography imaging reveals lobular heterogeneities in pancreatic islet and beta-cell mass

514   distribution. *Islets* 3, 204-208, doi:10.4161/isl.3.4.16417 (2011).

515 30 Deerinck, T. J., Bushong, E. A., Thor, A. & Ellisman, M. H. *NCMIR methods for 3D*

516   *EM: A new protocol for preparation of biological specimens for serial block face*

517   *scanning electron microscopy* <https://www.ncmir.ucsd.edu/sbem-protocol> (2010).

518 31 Saalfeld, S. *Linear stack alignment with SIFT. https://imagej.net/imagej-wiki-*

519   *static/Linear_Stack_Alignment_with_SIFT*, 2008).

520   32   Busse, B. & Miura, K. *MultiStackReg. https://biii.eu/multistackreg*, 2016).

521

536

546

Author contributions:

548   NC, SMAW, ES, JZ, LAC, UA, DM and AKÖ conceptualized the manuscript. NC, SMAW, ES,

549   MH, FM, JZ, EN and DW developed methodology and carried out the experiments. LAC, UA,

550   DM and AKÖ provided supervision and critical evaluation with the manuscript. NC, SMAW, ES,

551   LAC, UA, DM and AKÖ wrote the original draft of the manuscript and all authors reviewed and

552   edited the manuscript.

553

Competing interests:

555   Authors declare that they have no competing interests.

556

Materials and Correspondence:

558   Raw data can be obtained upon request (address AKÖ, anna.overby@umu.se)

559

560 **Figures:**


561
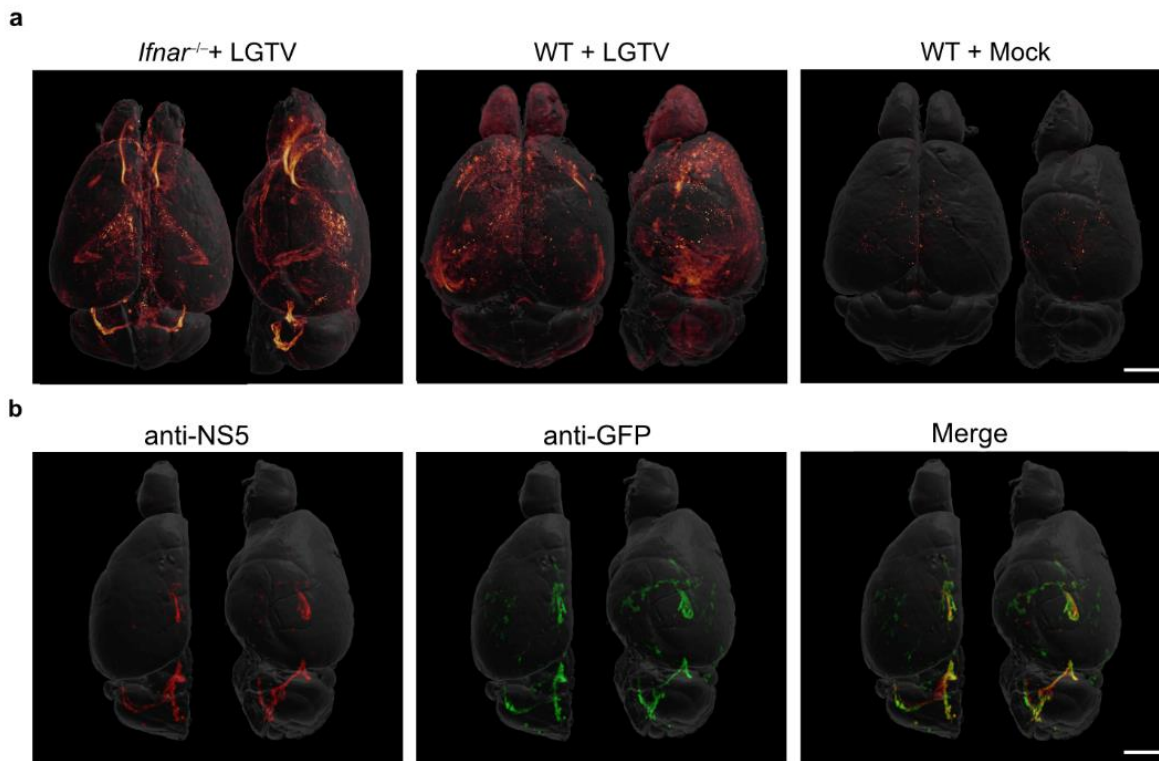
Fig. 1. OPT reveals the distribution of LGTV infection in the adult mouse brain shaped by type I IFN response. **a** Volumetric 3D-render of the brain of mock and LGTV infected mouse immunolabeled with anti-NS5 (virus marker; red glow) antibody. The signal intensity was normalized within an individual brain and adjusted to identical minimum and maximum. Five mice per group were analyzed and representative images are shown. The brain images for the remaining animals (n = 4 per group) are shown in Supplementary Fig. 2. For each image pair, the top and lateral views of the same specimen are shown. **b** Volumetric 3D-render of a half of brain from *Ifnar*$^{-/-}$ mouse infected with LGTV-GFP. The brain was immunolabeled with anti-NS5 (red) and anti-GFP antibodies (green). Signal overlap is shown in the merge image. Anatomical outlines were created by iso-surface rendering of autofluorescence signals. All scale bars = 2000 µm.
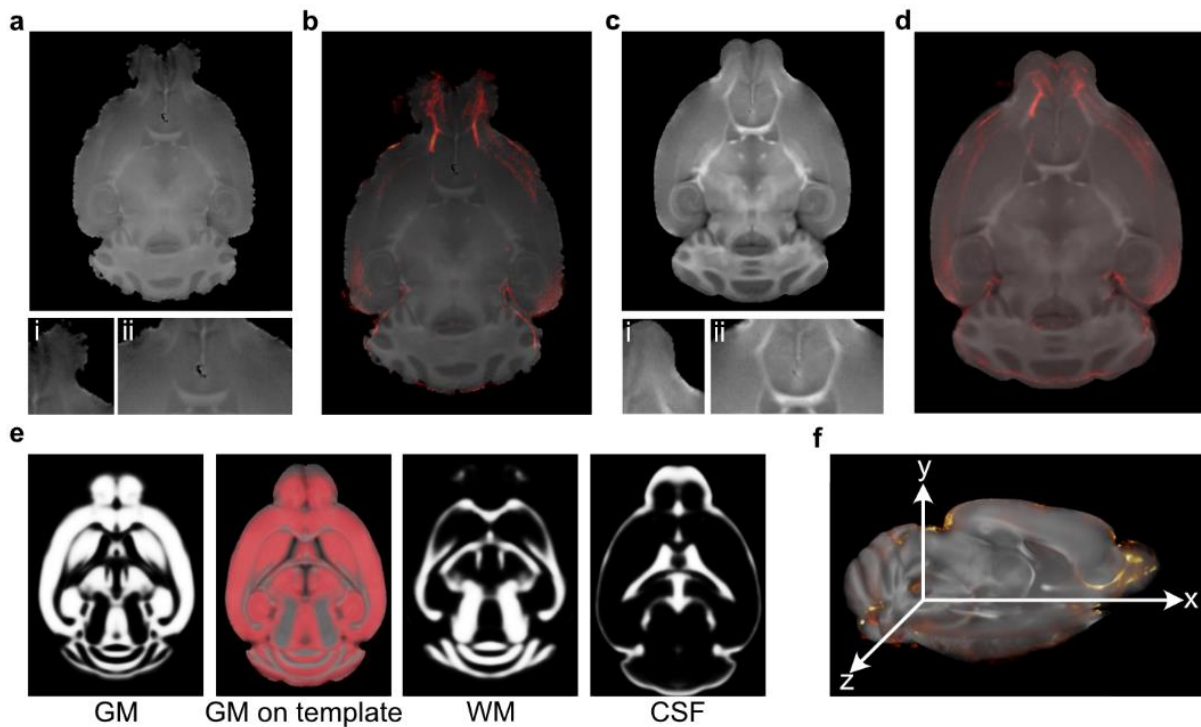
Fig. 2. OPT-MRI coregistration and template creation. **a** Sectional image of a single-subject MRI with insets showing zoomed image at (i) olfactory bulb and (ii) anterior commissure. **b** Fusion image created using viral OPT signal (red) with own MR scan. **c** Sectional image of the developed MRI brain template with insets showing zoomed image at (i) olfactory bulb and (ii) anterior commissure, showing improved anatomical details compared to own MR (a). **d** Fusion images created using viral OPT signal (red) with the template. **e** Study-specific tissue probability maps, perfectly fitting the template. GM, gray matter; WM, white matter; CSF, cerebrospinal fluid. **f** Detailed anatomical mapping of viral OPT signal with the template in 3D.
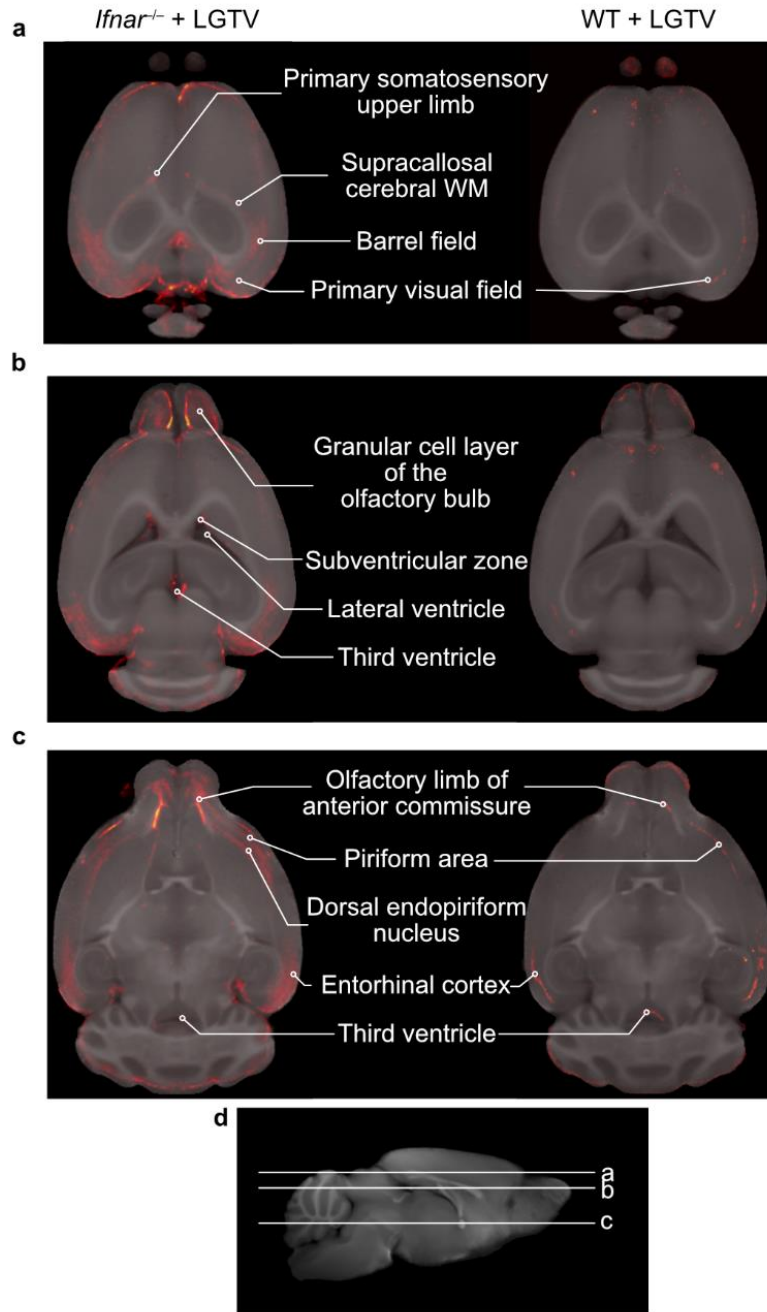
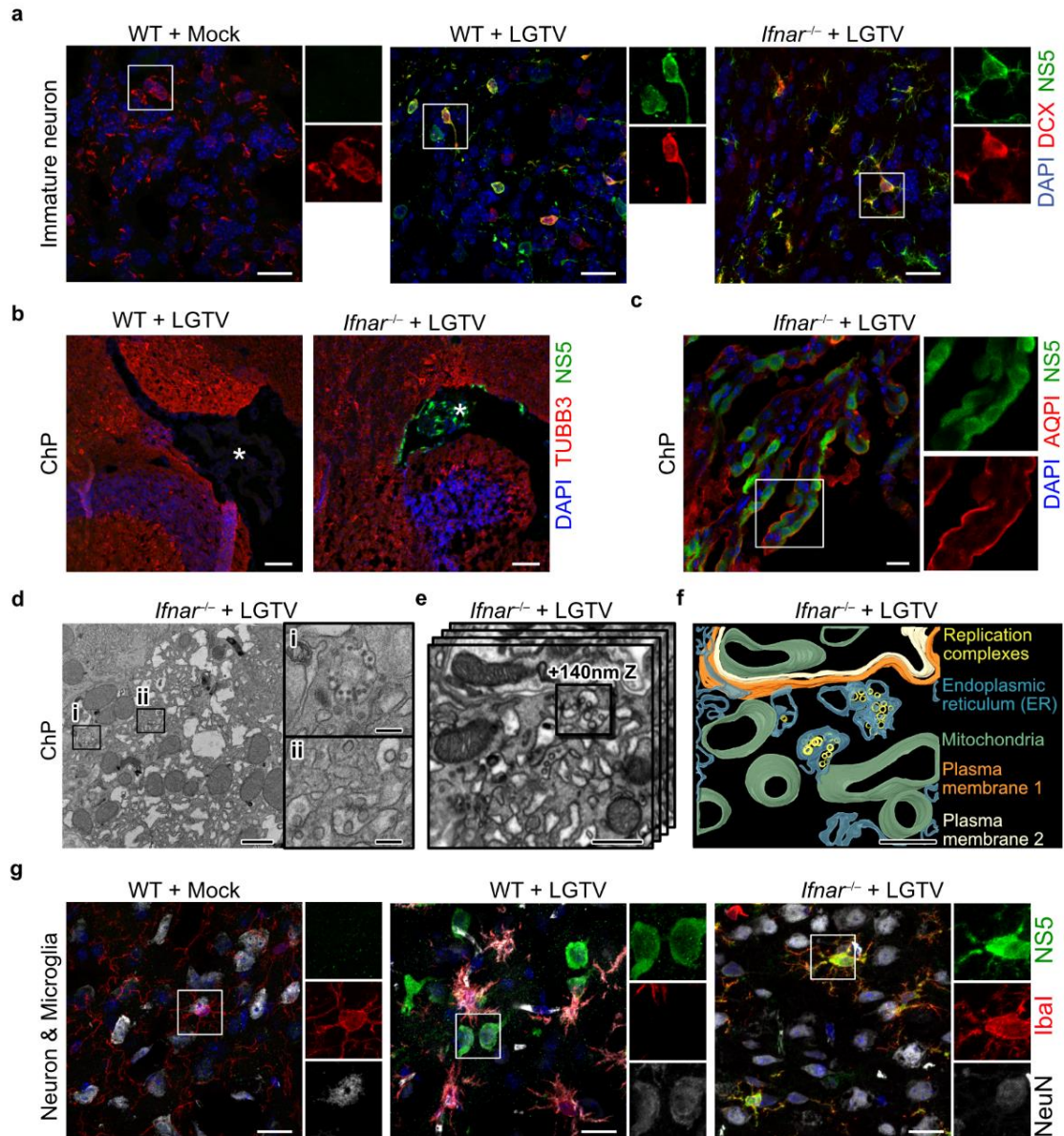**Fig. 3.** Brain mapping of viral signal using the developed OPT-MR fusion approach. **a-c** Anatomical mapping of brain regions after coregistration of viral OPT signal (red) with the study-specific MR brain template (gray). **d** Schematic illustration of slices of the brain template shown in A–C, viewed from the sagittal plane.

Fig. 4. Validation of LGTV infection in mouse brain using confocal and electron microscopy. **a** Maximum-intensity projection of confocal *z*-stack captured at olfactory bulb from sagittal brain sections (10 µm). The sections were immunolabeled using antibodies against viral NS5, immature neuron from rostral migratory stream (DCX) and the nucleus (DAPI). Scale bars = 20 µm. **b** Confocal microscopy images of infected cells in the fourth ventricle ChP (indicated by asterisk), immunolabeled with antibodies against NS5 and mature neuron (TUBB3). Scale bars = 100 µm. **c**

594 Fourth ventricle ChP were immunolabeled with antibodies against NS5 and ChP epithelial cell

595 (AQPI). Scale bars = 20 µm. **d** TEM images of brain sections fixed in resin. The image captured

596 a heavily infected cell indicated by dilated ER membrane, as compared to ER membrane of

597 uninfected ChP shown in Supplementary Fig. 3D. Scale bar = 1 µm. Insets show high

598 magnification images of (i) virus particles and (ii) replication complexes within dilated ER. Scale

599 bar = 200 nm. **e** FIB-SEM volume imaging shows viral replication complexes within dilated ER.

600 Scale bar = 500 nm. **f** Segmentation image created from the 3D volume images in (e). Scale bar =

601 500 nm. **g** Maximum-intensity projection of confocal z-stack captured at cerebral cortex from

602 sagittal brain sections (10 µm). The sections were immunolabeled using antibodies against viral

603 NS5, mature neuron (NeuN) and microglia (IbaI). The images are representative of at least 3

604 biological replicates for confocal images and 2 biological replicates with 3-5 technical replicates

605 for TEM and FIB-SEM. Scale bars = 20 µm.